Electronic Supplementary Information

Elucidating the Chirality Transfer Mechanisms During Enantioselective Synthesis for the Spin-Controlled Oxygen Evolution Reaction

Hayoung Im, Sunihl Ma, Hyungsoo Lee, Jaemin Park, Young Sun Park, Juwon Yun, Jeongyoub Lee, Subin Moon and Jooho Moon*

*E–mail: jmoon@yonsei.ac.kr

Keywords: CISS, chirality transfer, chiral inorganic oxide, oxygen evolution reaction, photoelectrochemical water splitting

Supplementary Figures

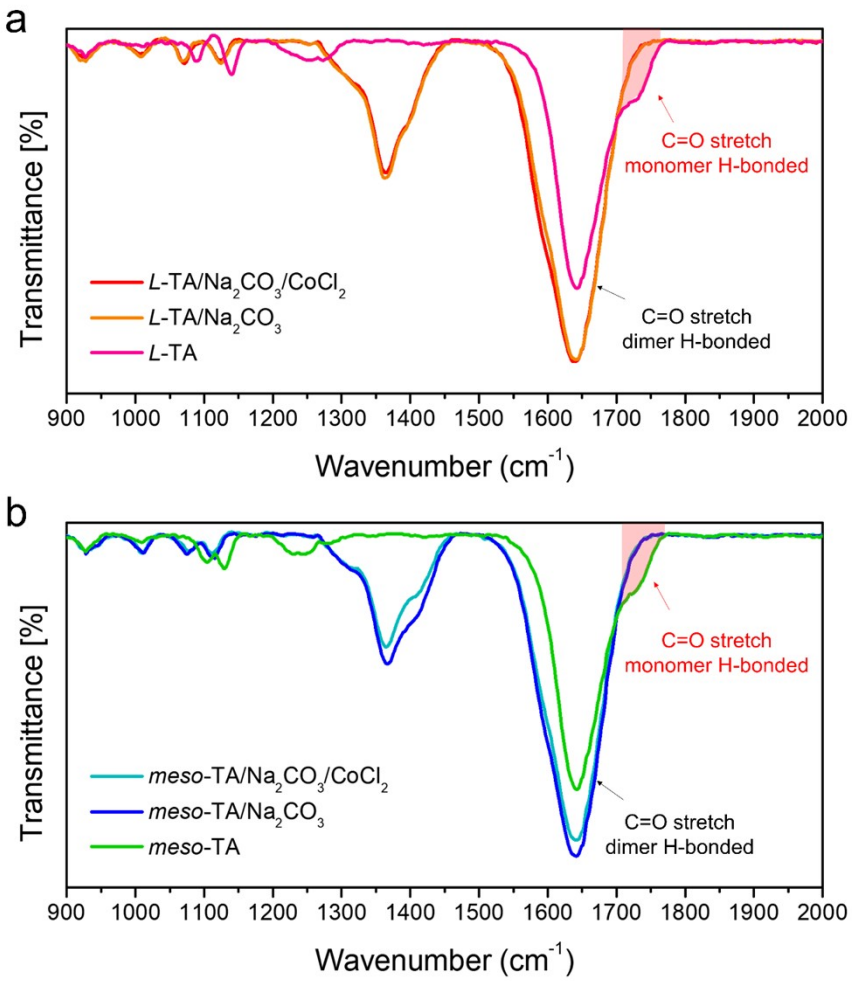

Figure S1. Full FTIR spectra of a) *L*-TA/Na_2CO_3/$CoCl_2$ and b) *meso*-TA/Na_2CO_3/$CoCl_2$ mixtures.

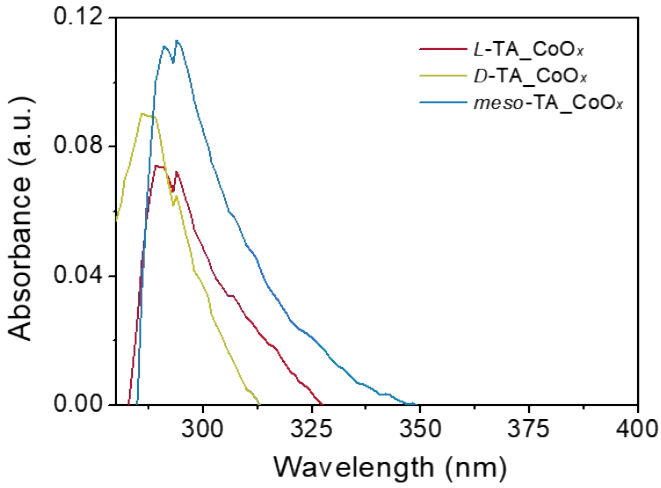

Figure S2. Absorbance of the *L*/*D*/*meso*-TA_CoO_x solution precursor.

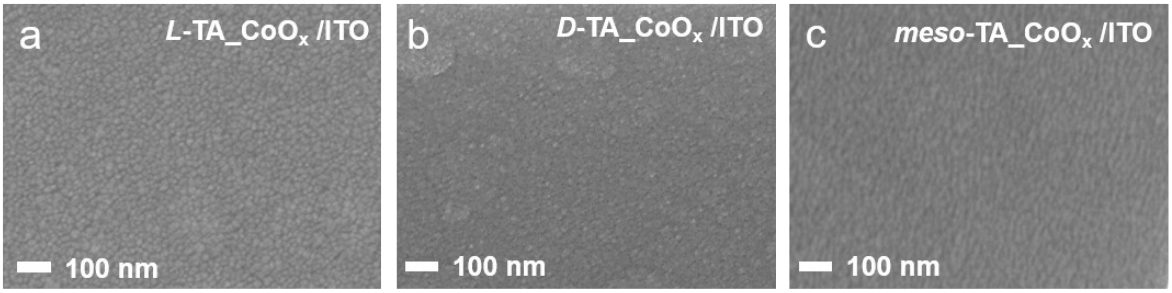

Figure S3. SEM images of a) *L*-TA_CoO_x, b) *D*-TA_CoO_x, and c) *meso*-TA_CoO_x films on an ITO substrate.

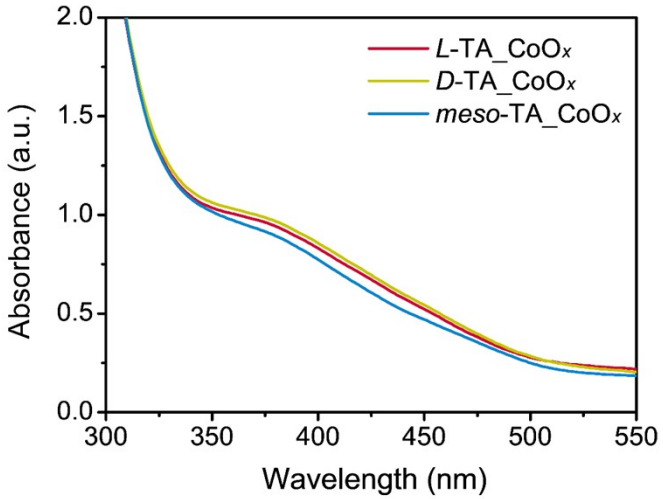

Figure S4. Absorbance of the *L*/*D*/*meso*-CoO_x thin films on an ITO substrate.

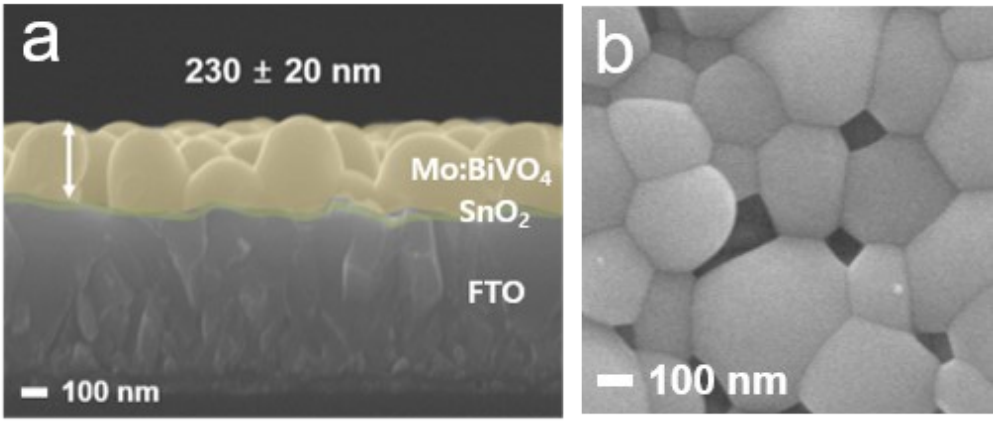

Figure S5. a) Cross-sectional SEM image and b) plain-view image of a bare BVO sample.

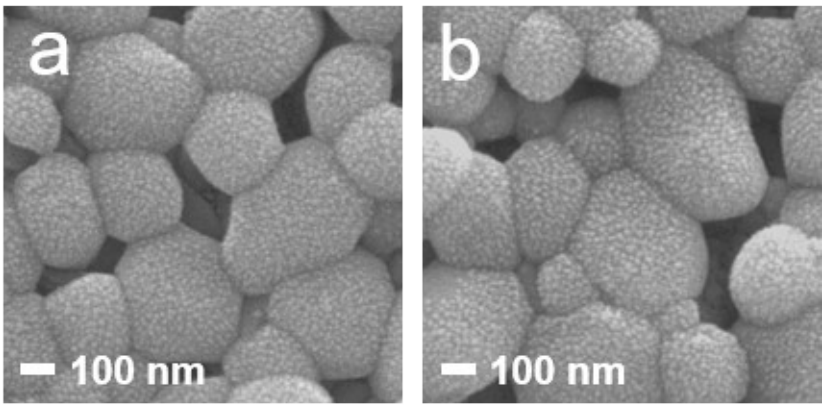

Figure S6. SEM images of a) *L*-TA_CoO_x/BVO and b) *meso*-TA_CoO_x/BVO.

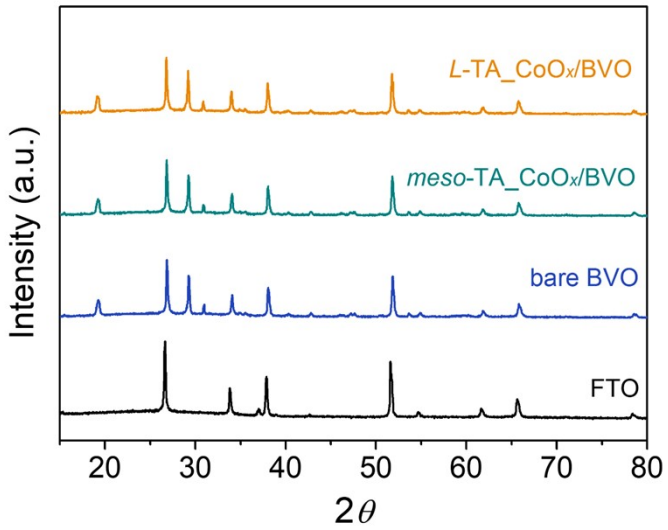

Figure S7. XRD patterns for the *L*-TA_CoO_x/BVO, *meso*-TA_CoO_x/BVO, and bare BVO films.

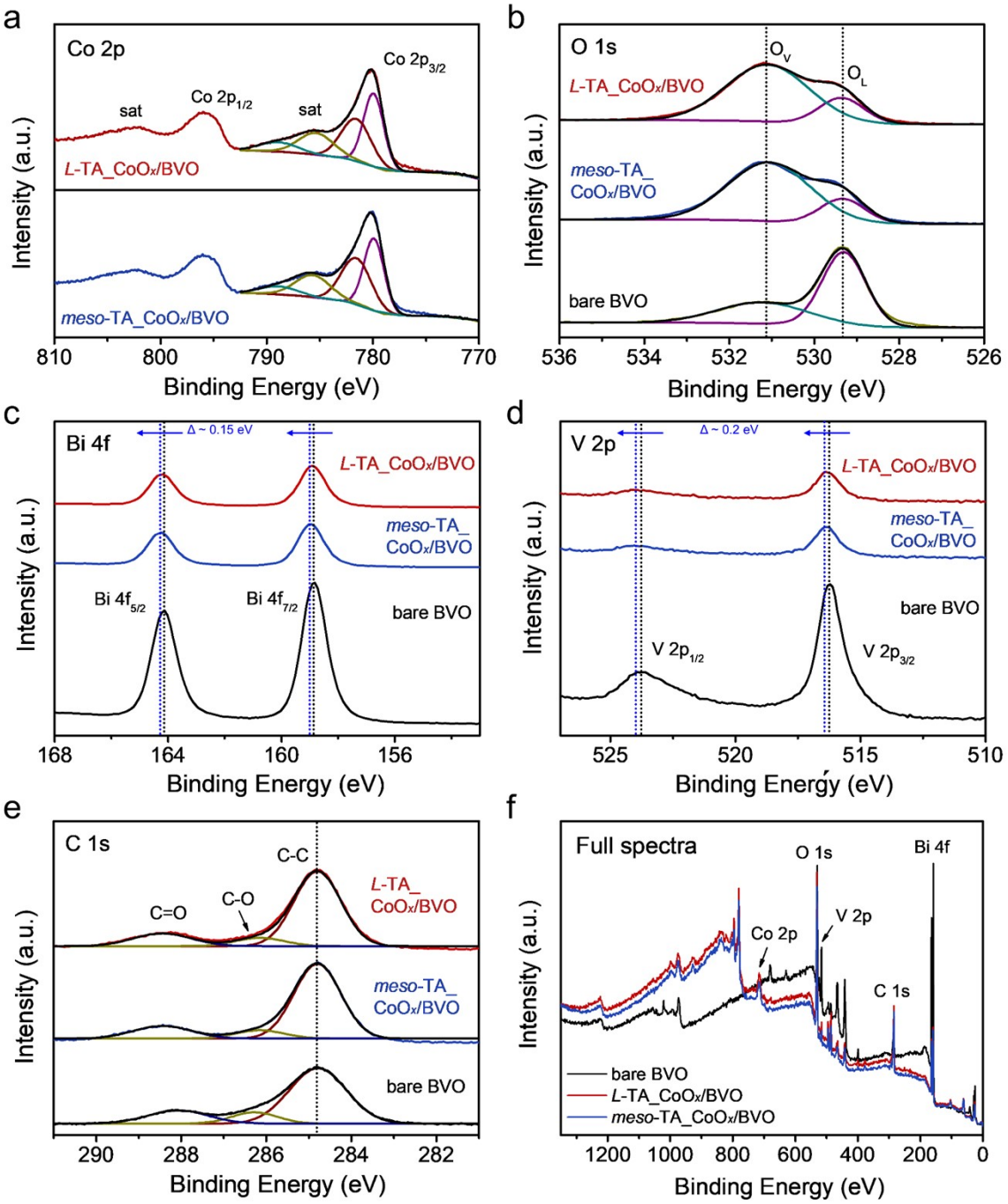

Figure S8. XPS spectra for the *L*-TA_CoO_x/BVO, *meso*-TA_CoO_x/BVO, and bare BVO films: a) Co 2p, b) O 1s, c) Bi 4f, d) V 2p, e) C 1s, and f) full spectra.

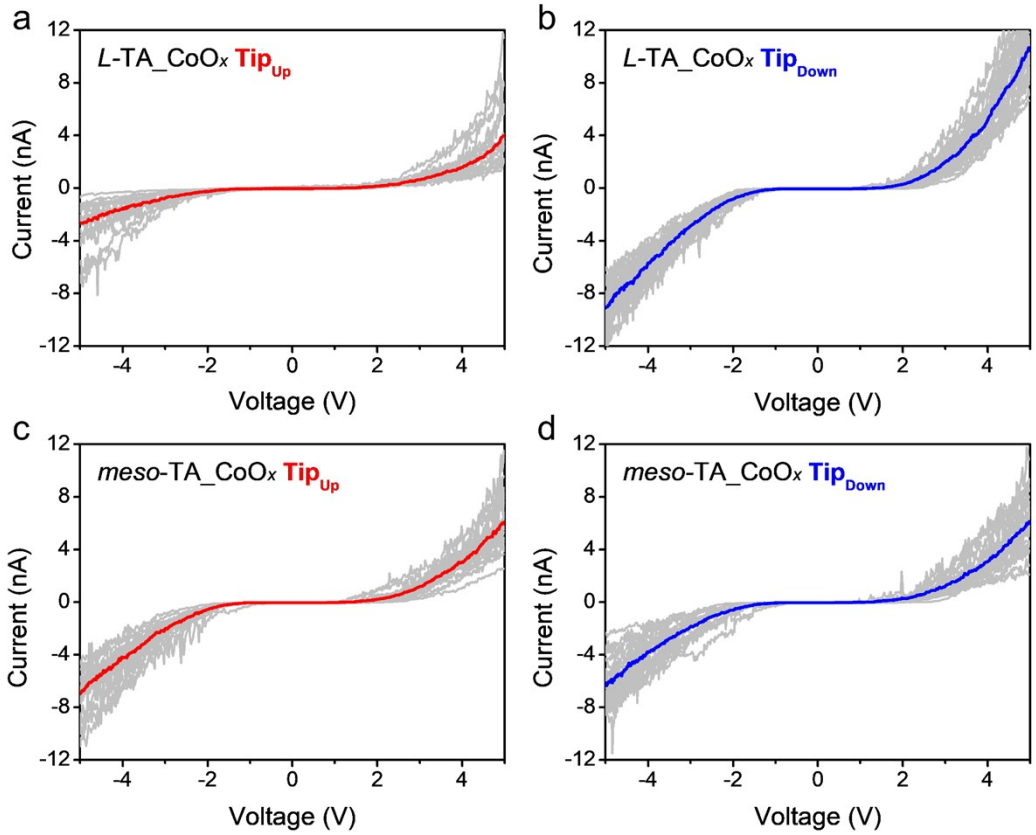

Figure S9. Raw data for the I-V curves recorded using magnetic conductive-probe AFM magnetized along the up or down magnetic field orientation at different positions: a-b) *L*-TA_CoO_x film and c-d) *meso*-TA_CoO_x film.

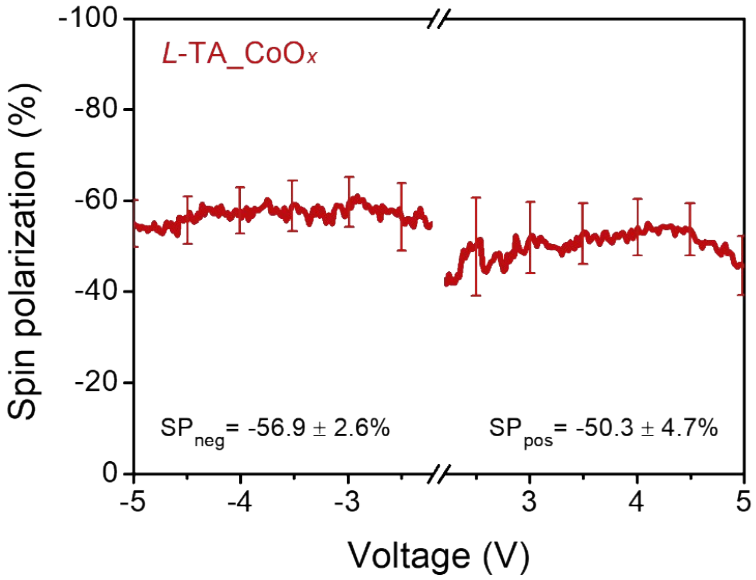

Figure S10. Calculated spin polarization as a function of the applied bias for the *L*-TA_CoO_x film scanned from –5 to 5 V. The error bars indicate the standard deviation.

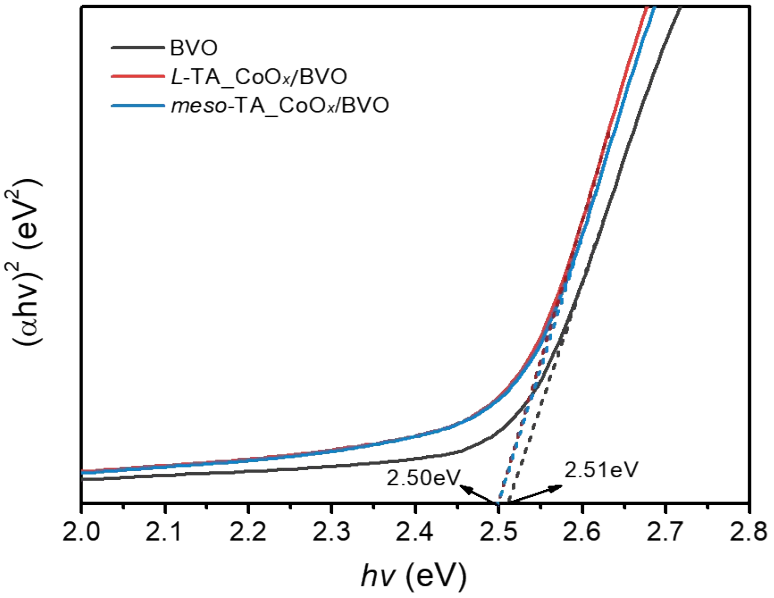

Figure. S11. Tauc plot of *L*-TA_CoO_x/BVO, *meso*-TA_CoO_x/BVO, and bare BVO.

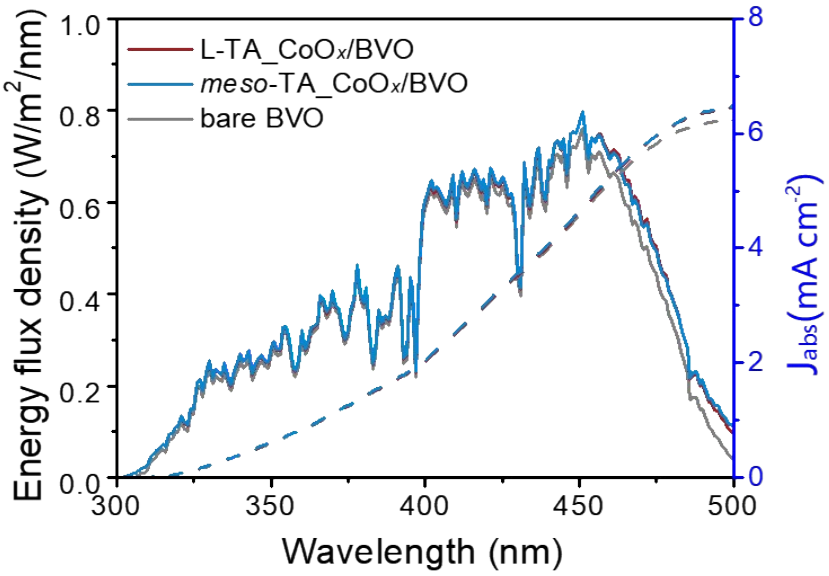

Figure S12. Estimated maximum absorbed photocurrent based on the light absorption (J_{abs}) calculated from the spectral radiance at AM 1.5G as well as the assumption of APCE=100%. The maximum absorbed photocurrent was estimated to 6.412 mA cm^{-2} for *meso*-TA_CoO_x/BVO and 6.413 mA cm^{-2} for *L*-TA_CoO_x/BVO.

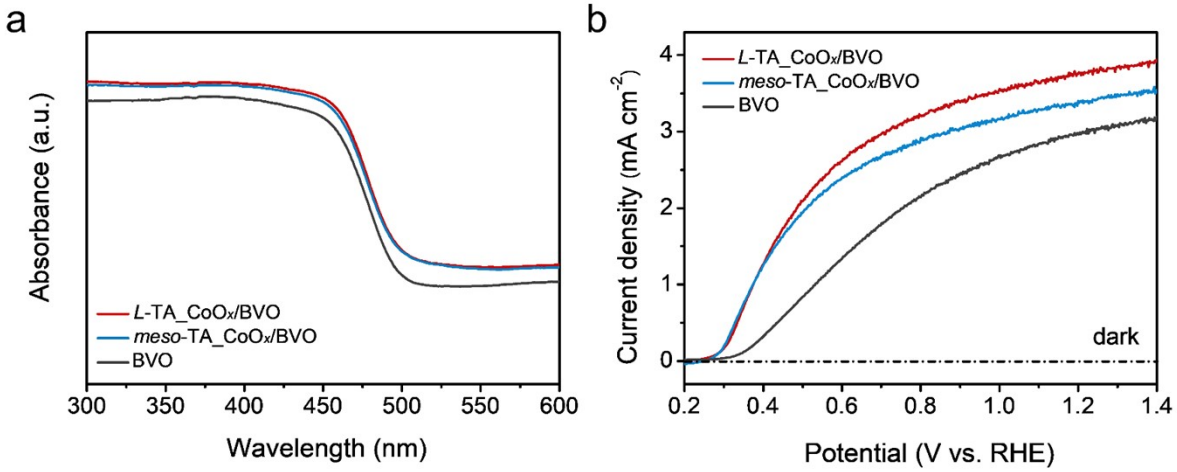

Figure S13. a) Absorbance of *L*-TA_CoO_x/BVO, *meso*-TA_CoO_x/BVO. b) SOR current density for *L*-TA_CoO_x/BVO, *meso*-TA_CoO_x/BVO, and bare BVO measured in 1 M KBi containing 0.2 M Na_2SO_3 (pH 9.0) under front-side 1-sun illumination at a scan rate of 20 mV s^{-1}.

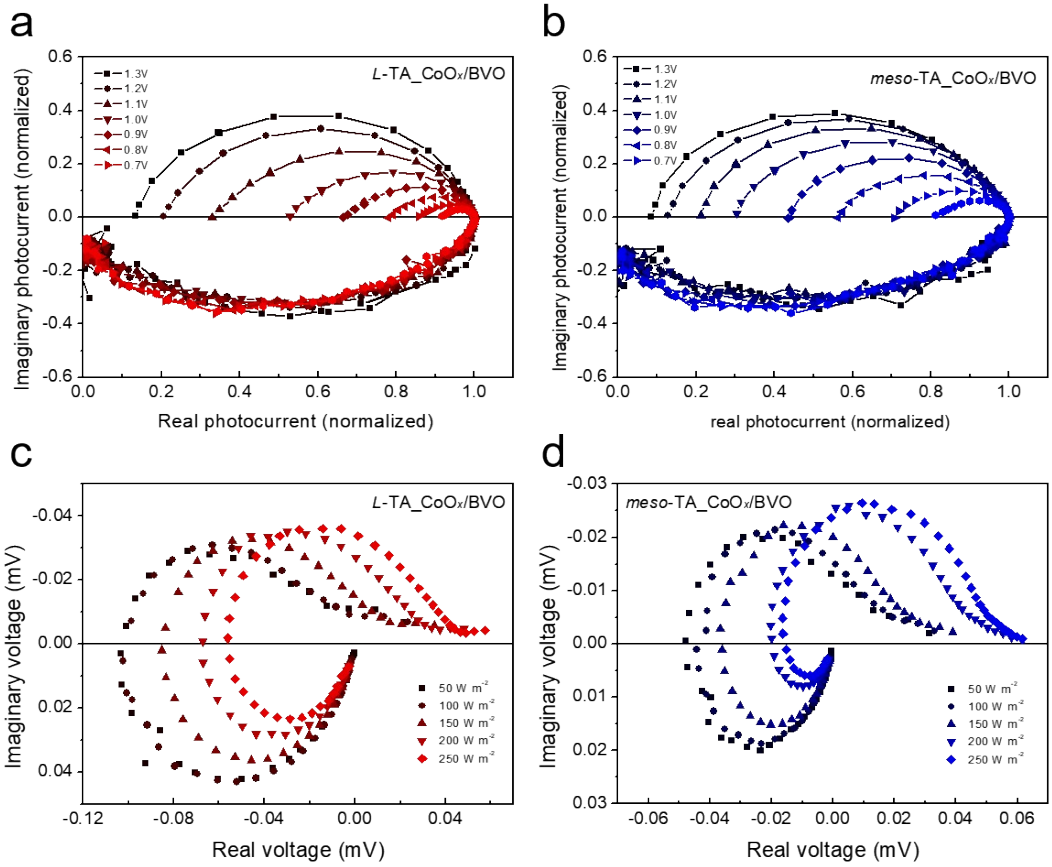

Figure S14. Raw data for the IMPS spectra measured in a 1.0 M KBi electrolyte (pH 9) at various potentials for the a) *L*-TA_CoO_x/BVO and b) *meso*-TA_CoO_x/BVO photoanodes. Raw data for the IMVS response measured in a 1.0 M KBi electrolyte (pH 9) under various illumination intensities for the c) *L*-TA_CoO_x/BVO and d) *meso*-TA_CoO_x/BVO photoanodes.

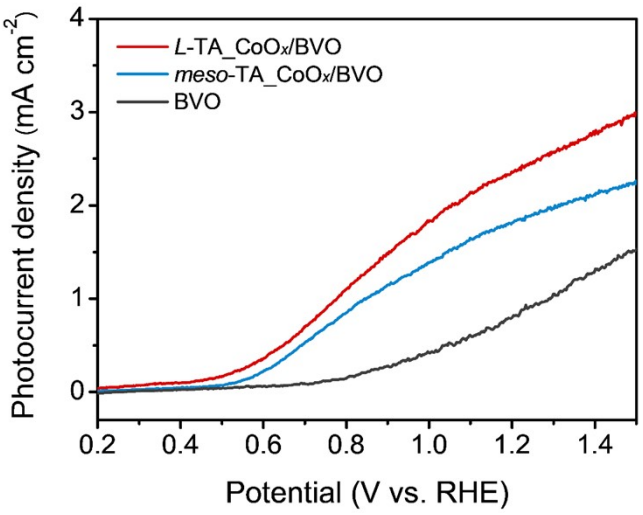

Figure S15. Current density–voltage (J-V) plots for all BVO samples measured in a 0.1 M Na_2SO_4 solution (pH 6.5) under AM 1.5 G illumination (100 mW cm^{-2}) with a scan rate of 15 mV s^{-1}.

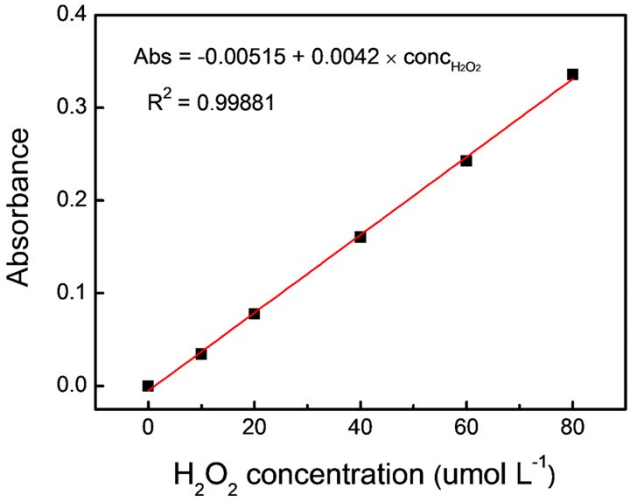

Figure S16. Calibration curve for commercial hydrogen peroxide as a function of its concentration.

Table S1. Frequencies of the IR absorption maxima of C-O bond in spectra of *L*/*meso*-TA and *L*/*meso*-TA/Na_2CO_3/$CoCl_2$ solution.

	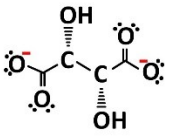	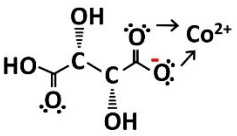	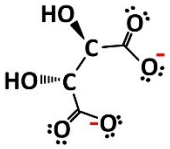	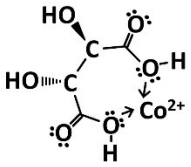
	L-(+)-TA	*L*-(+)-TA · Na_2CO_3 · $CoCl_2$	*meso*-TA	*meso*-TA · Na_2CO_3 · $CoCl_2$
ν_s(C–O)	1089 cm^{-1}	1070 cm^{-1}	1104 cm^{-1}	1079 cm^{-1}
ν_{as}(C–O)	1140 cm^{-1}	1123 cm^{-1}	1130 cm^{-1}	1112 cm^{-1}